Quantum Electronics **42** (8) 701–713 (2012)

NANOPHOTONICS

PACS numbers: 78.67.Bf; 78.67.Sc; 81.07.–b
DOI: 10.1070/QE2012v042n08ABEH014833

Plasmon–exciton coupling effects in light absorption and scattering by metal/J-aggregate bilayer nanoparticles

V.S. Lebedev, A.S. Medvedev

Abstract. **This paper examines plasmon–exciton coupling effects in light absorption and scattering by hybrid nanoparticles consisting of a metallic core and organic dye J-aggregate shell. The spectroscopic characteristics of such particles are calculated using generalised Mie theory for two concentric spheres in a wide spectral range for various geometric parameters of the system, core materials (Ag, Au, Cu and Al) and cyanine dyes (TC, OC and PIC). We determine the eigenfrequencies of hybrid modes in the system and photoabsorption peak heights as functions of the oscillator strength of the transition in the J-band of the dye, core radius and shell thickness, and demonstrate that the interactions of a Frenkel exciton with dipole and multipole plasmons have radically different effects on the optical properties of the composite nanoparticles. Varying the particle size and the optical constants of the core and shell materials influences the number of peaks in the spectra of the particles and leads to a significant redistribution of peak heights. We identify regions where the extinction spectrum of the particles is dominated by light absorption or scattering processes.**

Keywords: *optics of nanostructures, core–shell composite nanoparticles, localised plasmons, molecular J-aggregates, Frenkel excitons, plasmon–exciton coupling.*

1. Introduction

The study of the optical properties of hybrid nanomaterials is of interest for a number of fundamental issues in nanooptics and for applied research and technological projects aimed at creating next-generation optoelectronic and photonic devices such as light-emitting diodes [1], photovoltaic cells [2] and photonic switches [3]. Knowledge of the optical properties of hybrid nanostructures and a detailed understanding of the effects resulting from their interaction with light are crucial for a number of advanced applications of near-field optics [4, 5]. Composite nanostructures are used in studies concerned with nanolasers and stimulated emission of plasmon polaritons [6–9].

V.S. Lebedev P.N. Lebedev Physics Institute, Russian Academy of Sciences, Leninsky prosp. 53, 119991 Moscow, Russia; Moscow Institute of Physics and Technology (State University), Institutskii per. 9, 141700 Dolgoprudnyi, Moscow region, Russia;
e-mail: vlebedev@sci.lebedev.ru;
A.S. Medvedev Moscow Institute of Physics and Technology (State University), Institutskii per. 9, 141700 Dolgoprudnyi, Moscow region, Russia

Received 20 February 2012; revision received 21 May 2012
Kvantovaya Elektronika **42** (8) 701–713 (2012)
Translated by O.M. Tsarev

Recent years have seen increasing research interest in the optical properties of various metal/insulator and metal/semiconductor composite nanostructures [10]. The optical properties of metallic nanoparticles are well-known. Metal-containing hybrid nanoparticles possess a number of unique features. An interesting example of hybrid nanoparticles is metallic nanoshells consisting of an insulator core (e.g. SiO_2) and thin noble-metal shell [11]. The optical properties of such nanoparticles have been the subject of a number of studies (see e.g. Refs [12, 13]). The results demonstrate that varying the ratio of the shell thickness to the particle radius allows the frequencies of the plasmon modes of the nanoshell to be tuned over a wide spectral range, from the IR to UV.

This paper addresses the optical properties of another type of nanoparticle, in the form of a metallic core coated with a thin molecular J-aggregate layer (Fig. 1). J-aggregates are nanoclusters of noncovalently bonded organic dye molecules in which electronic excitations of individual molecules become delocalised by virtue of translational order, forming Frenkel excitonic states [14]. Kometani et al. [15] demonstrated the formation of cyanine dye J-aggregates on a spherical surface of noble-metal (Ag and Au) nanoparticles in an aqueous solution. This opened up the possibility of studying the electromagnetic coupling between the organic shell and metallic core of such nanoparticles and, hence, assessing the influence of plasmon–exciton interaction on the optical properties of metal/J-aggregate nanoparticles. The structure and spectroscopic properties of ~10-nm-diameter hybrid nanoparticles consisting of a metallic (Ag or Au) core and ~1-nm-thick TC cyanine dye J-aggregate monolayer have been the subject of extensive experimental studies [16–22]. The absorption spectra of silver and gold nanoparticles coated with TC dye J-aggregates in an aqueous solution were analysed theoretically [19–22] in the quasi-static approximation using a simple model for the dipole polarisability of two concentric spheres. Such an approach is only justified in the case of very small particles ($r \lesssim 10$ nm).

In addition to the above two-component spherical nanoparticles of small radius ($r \sim 5$ nm), two- and three-component nanostructures of various shapes and considerably larger dimensions (15–150 nm), containing a metallic core and external J-aggregate shell, were synthesised in a number of studies [23–26]. Interest in such hybrid nanostructures stems from the fact that increasing their size leads to an increase in plasmon–exciton coupling constant and significantly modifies the nature of the coupling, which as a result does not reduce to the interaction of a Frenkel exciton with a localised dipolar plasmon. Such composite nanostructures have rather complex absorption and scattering spectra, which result from the interaction of an exciton with multipole plasmons of different orders. The spectroscopic and nonlinear optical properties

of metal–insulator hybrid nanostructures and the effects resulting from their interaction with light are of considerable interest for a variety of applications, including biology [27,28] and the development of organic light-emitting diodes [29], photodetectors and solar cells [30,31].

In this paper, we present detailed calculations of the spectroscopic characteristics of two-component metal/J-aggregate nanoparticles in a wide spectral range for various geometric parameters of the system, core materials (Ag, Au, Cu and Al) and cyanine dyes. The J-aggregate-forming dyes used as shell materials – TC (3,3′-disulfopropyl-5,5′-dichlorothiacyanine sodium salt), OC (3,3′-disulfopropyl-5,5′-dichlorooxacyanine triethylammonium salt) and PIC (1,1′-disulfopropyl-2,2′-cyanine triethylammonium salt) – have absorption peaks in different spectral regions relative to their plasmon resonance peaks and differ drastically in the oscillator strength of transitions in their J-band. As a result, they differ qualitatively in the nature of the interaction of a Frenkel exciton with localised plasmons and differ in the influence of this interaction on the spectral characteristics of the nanosystems in the weak and strong plasmon–exciton coupling regimes. In our calculations, we vary the particle core radius from 5 to 65 nm, the shell thickness from 1 to 5 nm and the wavelength from the UV to near-IR spectral region. In this situation, the simple formulas of the quasi-static approximation are inapplicable, so we perform calculations using generalised Mie theory for bilayer particles, which is modified by taking into account the size effect on the dielectric permittivity of the core due to free electron scattering by the spherical metal/J-aggregate interface. The permittivity of the shell is treated within the anharmonic oscillator model with a reduced oscillator strength of the transition in the J-band.

One of our main purposes here is to demonstrate qualitative differences in the nature of the interaction of localised plasmons in the metallic core of a hybrid particle with a molecular Frenkel exciton in the J-aggregate shell and to assess its influence on the absorption and scattering spectra of the nanoparticles. To this end, we constructed an analytical model for determining the frequencies of hybrid modes in a composite system and numerically calculated the spectral position and maximum heights of photoabsorption peaks of the nanoparticles. We examined the dependences of these quantities on the reduced oscillator strength of the transition in the J-band, core radius and shell thickness. The results indicate that these parameters determine the nature of plasmon–exciton coupling in the system. We identified boundaries between regions where light absorption and scattering processes prevail. The present results provide further insight into the optical properties of the hybrid nanoparticles in question and the efficiency of the coupling between a Frenkel exciton in molecular dye J-aggregates and dipole and multipole plasmons localised in the metallic core of the nanoparticles.

2. General formulas for the multipole expansion of the contributions of TM and TE modes to the light absorption and scattering cross sections of bilayer particles

Below, we present exact formulas for the light absorption and scattering cross sections of a two-component spherical nanoparticle, which are valid at any relationship between the wavelength and total particle radius. Figure 1 shows a schematic representation of a hybrid particle with a core radius r_1 and shell thickness $l = r_2 - r_1$, surrounded by an inert medium of dielectric permittivity $\varepsilon_h(\omega)$ and magnetic permeability $\mu_h = 1$. The materials of the concentric spherical layers are assumed to be uniform and isotropic, with frequency-dependent complex permittivities $\varepsilon_1(\omega)$ and $\varepsilon_2(\omega)$ and magnetic permeabilities $\mu_1 = \mu_2 = 1$. The field strength of a linearly polarised monochromatic plane wave incident on the particle is proportional to $\exp(-i\omega t + ik_h z)$. The incident wave is partially scattered and absorbed by the particle. The Mie's exact theory of light absorption and scattering by a uniform sphere (see e.g. Ref. [32]) was generalised to two-component spherical particles first in Refs [33,34] and then in Refs [35,36], using standard boundary conditions for fields at $r = r_1$ and $r = r_2$.

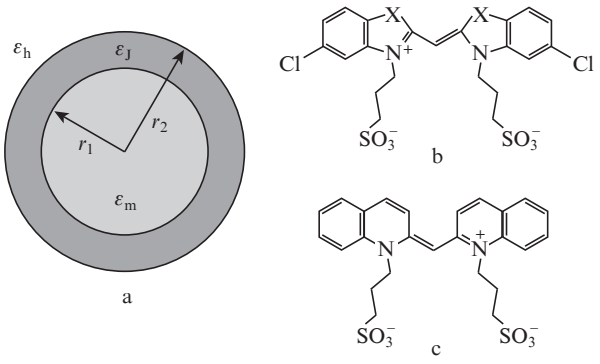

Figure 1. (a) Schematic representation of a particle consisting of a metallic core of permittivity ε_m and a J-aggregate shell of permittivity ε_J and surrounded by a medium of permittivity ε_h. Molecular structures of the anionic cyanine dyes (b) TC (X = S), OC (X = O) and (c) PIC.

The general expressions for the light absorption and scattering cross sections (σ_{abs} and σ_{scat}) of a multilayer spherical particle and its total extinction cross section (σ_{ext}) can be represented in the same form as those for a uniform sphere [32]:

$$\sigma_{abs} = \frac{\pi}{2k_h^2}\sum_{n=1}^{\infty}(2n+1)(2-|2a_n-1|^2-|2b_n-1|^2), \qquad (1)$$

$$\sigma_{scat} = \frac{2\pi}{k_h^2}\sum_{n=1}^{\infty}(2n+1)(|a_n|^2+|b_n|^2), \qquad (2)$$

$$\sigma_{ext} = \frac{2\pi}{k_h^2}\sum_{n=1}^{\infty}(2n+1)\mathrm{Re}(a_n+b_n). \qquad (3)$$

Here, a_n and b_n are the coefficients in the expansion of the transverse electric (TE) and transverse magnetic (TM) modes of the scattered wave, respectively; n is the multipole order; and $k_h = \omega\sqrt{\varepsilon_h}/c$ is the magnitude of the wave vector in the medium around the particle. Particular expressions for the coefficients a_n and b_n and their values are determined by the specifics of the problem and depend on the geometry of the hybrid particle and the permittivities of the core, shell and medium.

In the case of spherical core–shell bilayer nanoparticles (Fig. 1), we rederived the general expressions for the complex coefficients a_n and b_n in the expansion of the scattered electromagnetic field using a theoretical approach developed earlier [33–36] and boundary conditions for fields at $r = r_1$ and $r = r_2$. It is convenient to represent the final expressions for a_n and b_n in the form

$$a_n = X_n^{(a)}/Y_n^{(a)}, \quad b_n = X_n^{(b)}/Y_n^{(b)}, \tag{4}$$

where the functions $X_n^{(a)}$, $Y_n^{(a)}$, $X_n^{(b)}$ and $Y_n^{(b)}$ can be expressed in compact form through determinants. The explicit expressions for the functions $X_n^{(a)}$ and $Y_n^{(a)}$, which determine the contribution of the TE mode of order n, have the form

$$X_n^{(a)} = \begin{vmatrix} j_n(k_1r_1) & j_n(k_2r_1) & y_n(k_2r_1) & 0 \\ u_n'(k_1r_1) & u_n'(k_2r_1) & v_n'(k_2r_1) & 0 \\ 0 & j_n(k_2r_2) & y_n(k_2r_2) & j_n(k_hr_2) \\ 0 & u_n'(k_2r_2) & v_n'(k_2r_2) & u_n'(k_hr_2) \end{vmatrix}, \tag{5}$$

$$Y_n^{(a)} = \begin{vmatrix} j_n(k_1r_1) & j_n(k_2r_1) & y_n(k_2r_1) & 0 \\ u_n'(k_1r_1) & u_n'(k_2r_1) & v_n'(k_2r_1) & 0 \\ 0 & j_n(k_2r_2) & y_n(k_2r_2) & h_n^{(1)}(k_hr_2) \\ 0 & u_n'(k_2r_2) & v_n'(k_2r_2) & w_n'(k_hr_2) \end{vmatrix}. \tag{6}$$

Here, $k_1 = \omega\sqrt{\varepsilon_1}/c$ and $k_2 = \omega\sqrt{\varepsilon_2}/c$ are the magnitudes of the wave vectors of the light in the core and shell, respectively; $\varepsilon_1 \equiv \varepsilon_m(\omega)$ and $\varepsilon_2 \equiv \varepsilon_J(\omega)$ are the complex permittivities of the metallic core and organic shell at the frequency of the incident light, ω; r_2 is the outer radius of the particle; $j_n(z)$, $y_n(z)$ and $h_n^{(1)}(z)$ are spherical Bessel, Neumann and Hankel functions; $u_n(z) = zj_n(z)$, $v_n(z) = zy_n(z)$ and $w_n(z) = zh_n^{(1)}(z)$ are spherical Riccati–Bessel, Riccati–Neumann and Riccati–Hankel functions; and primes denote differentiation of a function with respect to its argument.

Similarly, the final expressions for the functions $X_n^{(b)}$ and $Y_n^{(b)}$, which determine the contribution of the TM modes, can be represented in the form

$$X_n^{(b)} = \begin{vmatrix} j_n(k_1r_1) & \sqrt{\frac{\varepsilon_2}{\varepsilon_1}}j_n(k_2r_1) & \sqrt{\frac{\varepsilon_2}{\varepsilon_1}}y_n(k_2r_1) & 0 \\ u_n'(k_1r_1) & \sqrt{\frac{\varepsilon_1}{\varepsilon_2}}u_n'(k_2r_1) & \sqrt{\frac{\varepsilon_1}{\varepsilon_2}}v_n'(k_2r_1) & 0 \\ 0 & \sqrt{\frac{\varepsilon_2}{\varepsilon_h}}j_n(k_2r_2) & \sqrt{\frac{\varepsilon_2}{\varepsilon_h}}y_n(k_2r_2) & j_n(k_hr_2) \\ 0 & \sqrt{\frac{\varepsilon_h}{\varepsilon_2}}u_n'(k_2r_2) & \sqrt{\frac{\varepsilon_h}{\varepsilon_2}}v_n'(k_2r_2) & u_n'(k_hr_2) \end{vmatrix}, \tag{7}$$

$$Y_n^{(b)} = \begin{vmatrix} j_n(k_1r_1) & \sqrt{\frac{\varepsilon_2}{\varepsilon_1}}j_n(k_2r_1) & \sqrt{\frac{\varepsilon_2}{\varepsilon_1}}y_n(k_2r_1) & 0 \\ u_n'(k_1r_1) & \sqrt{\frac{\varepsilon_1}{\varepsilon_2}}u_n'(k_2r_1) & \sqrt{\frac{\varepsilon_1}{\varepsilon_2}}v_n'(k_2r_1) & 0 \\ 0 & \sqrt{\frac{\varepsilon_2}{\varepsilon_h}}j_n(k_2r_2) & \sqrt{\frac{\varepsilon_2}{\varepsilon_h}}y_n(k_2r_2) & h_n^{(1)}(k_hr_2) \\ 0 & \sqrt{\frac{\varepsilon_h}{\varepsilon_2}}u_n'(k_2r_2) & \sqrt{\frac{\varepsilon_h}{\varepsilon_2}}v_n'(k_2r_2) & w_n'(k_hr_2) \end{vmatrix}. \tag{8}$$

Combined with (1)–(3), Eqns (4)–(8) allow one to calculate not only the total absorption, scattering and extinction cross sections but also the contributions of individual terms in the multipole series that correspond to TM and TE modes of various orders.

3. Quasi-static approximation

When the particle radius is much less than the wavelength of the light, we can use the quasi-static approximation and retain only the electric dipole term ($n = 1$). The expressions for the absorption and scattering cross sections then take the form [32]

$$\sigma_{abs}(\omega) = 4\pi k_h V \operatorname{Im}[\tilde{\alpha}(\omega)],$$
$$\sigma_{scat}(\omega) = \frac{8\pi}{3} k_h^4 V^2 |\tilde{\alpha}(\omega)|^2. \tag{9}$$

Here, $\tilde{\alpha} = \alpha/V$ is the effective polarisability per unit volume for a particle of volume V and polarisability α. The simplest expression is that for the dipole polarisability of a spherical metallic particle of permittivity ε_m [32]:

$$\tilde{\alpha} = \frac{3}{4\pi}\frac{\varepsilon_m - \varepsilon_h}{\varepsilon_m + 2\varepsilon_h}. \tag{10}$$

In the case of a bilayer spherical particle, ε_m in (9) and (10) should be replaced by the effective permittivity of the core–shell system, ε_2^{eff}, which is equivalent to the permittivity of a uniform sphere and can be found as [37]

$$\varepsilon_2^{eff} = \varepsilon_2 \frac{2[1-(r_1/r_2)^3] + [1+2(r_1/r_2)^3](\varepsilon_1/\varepsilon_2)}{[2+2(r_1/r_2)^3] + [1-(r_1/r_2)^3](\varepsilon_1/\varepsilon_2)}. \tag{11}$$

Thus, the effective dipole polarisability $\tilde{\alpha} = \alpha/V$ per unit volume of a bilayer particle is

$$\tilde{\alpha} = \frac{3}{4\pi}\frac{(\varepsilon_1-\varepsilon_2)(2\varepsilon_2+\varepsilon_h)(r_1/r_2)^3 + (\varepsilon_2-\varepsilon_h)(2\varepsilon_2+\varepsilon_1)}{2(\varepsilon_1-\varepsilon_2)(\varepsilon_2-\varepsilon_h)(r_1/r_2)^3 + (\varepsilon_2+2\varepsilon_h)(2\varepsilon_2+\varepsilon_1)}. \tag{12}$$

Combined with (9), this expression can be used to estimate the electric dipole contribution to the light absorption and scattering cross sections of small hybrid particles.

4. Dielectric permittivities

The permittivity of a noble metal can be expressed as the sum of the contributions of free and bound electrons: $\varepsilon(\omega) = \varepsilon_{intra}(\omega) + \varepsilon_{inter}(\omega)$. The free-electron contribution can be represented by the Drude formula:

$$\varepsilon_{intra}(\omega) = \varepsilon_m^\infty - \frac{\omega_p^2}{\omega^2 + i\omega\gamma_{intra}}. \tag{13}$$

Here, ω_p is the plasma frequency; γ_{intra} is the attenuation coefficient ($1/\gamma_{intra}$ is the relaxation time); and ε_m^∞ is the high-frequency permittivity of the metal. If the particle size is small compared to the electron mean free path in bulk metal, l_∞, then in calculating $\varepsilon_{intra}(\omega)$ one should take into account the size effect associated with free-electron scattering at the metal/J-aggregate interface. As a consequence, the attenuation coefficient γ_{intra} and, hence, permittivity ε_{intra} depend on both frequency and metallic core radius r_1. In this study, the effective attenuation coefficient will be represented by the phenomenological relation [38]

$$\gamma_{intra}^r = \gamma_{intra}^{bulk} + \xi\frac{v_F}{r_1}. \tag{14}$$

Here, v_F is the Fermi velocity; ξ is a dimensional constant of the order of unity, which can be evaluated from comparison with experimental data on light absorption by metallic particles; and γ_{intra}^{bulk} is the attenuation coefficient of bulk metal.

The contribution of bound electrons (electronic transitions between the d-valence band and sp-conduction band for the noble metals) can be evaluated within the random phase approximation [39]:

$$\varepsilon_{\text{inter}}(\omega) = K\int_{\omega_g}^{\infty} \mathrm{d}x \frac{\sqrt{x-\omega_g}}{x}[1-F(x,\Theta)] \times \frac{(x^2-\omega^2+\gamma_{\text{inter}}^2-2\mathrm{i}\omega\gamma_{\text{inter}})}{(x^2-\omega^2+\gamma_{\text{inter}}^2)^2+4\omega^2\gamma_{\text{inter}}^2}. \quad (15)$$

Here, $F(\omega,\Theta)$ is the electron energy ($\hbar\omega$) distribution function at temperature Θ, and γ_{inter} is the attenuation coefficient for interband transitions. Following Pines and Nozieres [39], we consider transitions between the dispersionless d-band and parabolic sp-conduction band with an electron effective mass m_* and minimum energy $\hbar\omega_g$ relative to the d-band. The constant in (15) is given by $K = 8D^2e^2m_*\sqrt{2m_*}/(\pi\hbar^3m_e^2)$, where D is the dipole moment of the transition, which can be evaluated using the oscillator strength sum rule. Note that the bound electron contribution (15) is only slightly influenced by the size effect. Therefore, the two contributions to the permittivity of the metallic core can be adequately described, with the size effect taken into account, by

$$\varepsilon_m(\omega,r) = \varepsilon_{\text{bulk}}(\omega) + \omega_p^2\left(\frac{1}{\omega^2+\mathrm{i}\omega\gamma_{\text{intra}}^{\text{bulk}}} - \frac{1}{\omega^2+\mathrm{i}\omega\gamma_{\text{intra}}^{\text{r}}}\right), \quad (16)$$

following an approach described in Kreibig and Vollmer [38]. Here, $\varepsilon_{\text{bulk}}$ is the permittivity of bulk metal evaluated from experimental data for Ag, Au, Cu [40] and Al [41].

In the anharmonic oscillator model, the dielectric function of a molecular exciton in a dye J-aggregate shell is given by

$$\varepsilon_J(\omega) = \varepsilon_J^{\infty} + \frac{f\omega_0^2}{\omega_0^2-\omega^2-\mathrm{i}\omega\Gamma}, \quad (17)$$

where ω_0 is the centre frequency of the transition; Γ is its linewidth; f is the reduced oscillator strength; and ε_J^{∞} is the permittivity far away from the centre of the J-band. The parameters of the Lorentzian profile of the dye J-band can be determined from experimental data. The parameters of J-aggregates of the cyanine dyes under consideration are presented in Table 1.

In this study, all cross sections were calculated for metal/J-aggregate hybrid nanoparticles in an aqueous solution. The permittivity of water, ε_w, varies little in the visible range ($1.77 < \varepsilon_w < 1.82$ in the range 350 nm $< \lambda <$ 700 nm) and can be determined from experimental data [42].

Table 1. Parameters of TC, OC and PIC cyanine dye J-aggregates.

Dye	ε_J^{∞}	ω_0/eV	λ_0/nm	f	Γ/eV	Ref.
TC	1	2.68	462.6	0.90	0.066	[15]
OC	1	3.04	407.2	0.01	0.039	[43]
PIC	2.9	2.13	582.1	0.10	0.033	[23, 44]

5. Key features in the absorption spectra of the hybrid nanoparticles

Below we discuss the key features in the absorption spectra of silver and gold nanoparticles coated with TC, OC and PIC cyanine dye J-aggregates. The absorption peaks in the J-band of such dyes are situated in different spectral regions relative to the plasmon resonance peaks of Ag and Au particles, and the dyes differ drastically in the oscillator strength of the transition (Table 1). Calculations were performed in a wide spectral range for various geometries of the composite system using the exact formulas given in Section 2 for light absorption and scattering cross sections and the permittivities of the metallic core and J-aggregate shell described in Section 4.

Figure 2 presents the photoabsorption cross sections calculated for Ag/TC and Au/TC hybrid particles in aqueous solution using the general formulas (1) and (4)–(8). The inner and outer radii of the concentric spheres were taken to be 20 and 23 nm, respectively. It is seen that, in the visible range, each spectrum has two well-defined peaks. The peaks of the Ag/TC particles are centred at $\lambda_{\text{Ag}}^{(1)} = 419$ nm and $\lambda_{\text{Ag}}^{(2)} = 482$ nm. For the Au/TC particles, we obtained $\lambda_{\text{Au}}^{(1)} = 543$ nm and $\lambda_{\text{Au}}^{(2)} = 387$ nm.

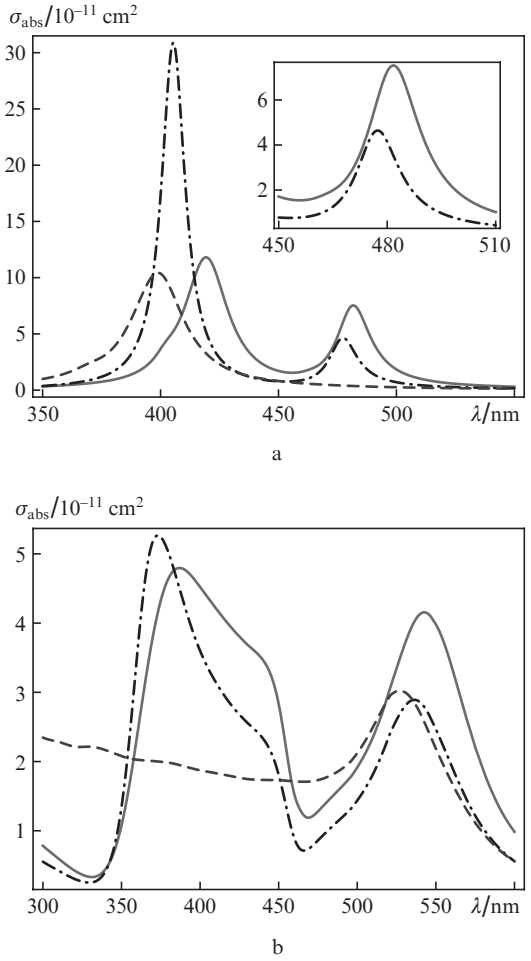

Figure 2. Photoabsorption cross section (σ_{abs}) as a function of wavelength in vacuum (λ) for (a) Ag/TC and (b) Au/TC particles in aqueous solution at a core radius $r_1 = 20$ nm and shell thickness $l = 3$ nm. The solid lines represent calculations by the exact formulas (1) and (4)–(8), the dot-dashed lines represent calculations in the quasi-static approximation [formulas (9) and (12)], and the dashed lines represent calculation results for uncoated silver and gold particles ($r = 20$ nm).

Comparison of the results presented in Figs 2a and 2b demonstrates characteristic differences between the absorption spectra of the particles containing silver and gold cores. The absorption peaks of the Ag/TC particles differ markedly in height. The position of the shorter wavelength peak approaches that of the localised dipole plasmon resonance peak of uncoated silver particles. At the geometric parameters under consideration, the redshift of the shorter wavelength peak (relative to

the absorption peak of uncoated silver particles) is $\Delta\lambda = 25$ nm. The longer wavelength absorption peak of the Ag/TC particles is shifted relative to the unperturbed centre wavelength λ_0 of the absorption peak of the TC dye J-aggregate by $\Delta\lambda = 20$ nm. The opposite situation occurs for the Au/TC particles. In this case, the longer wavelength peak of the composite system is redshifted ($\Delta\lambda = 17$ nm) relative to the peak of uncoated gold particles. The shorter wavelength peak is markedly shifted ($\Delta\lambda = 75$ nm) relative to the absorption peak of the TC J-aggregate (centred at $\lambda_{TC} = 462$ nm). The longer wavelength peak is slightly weaker than the shorter wavelength one. This is because plasmon–exciton coupling has different effects in the Ag/TC and Au/TC systems and because there are different relationships between the excitation energy of a Frenkel exciton in the TC dye shell and the plasmon resonance energies in Ag and Au (the absorption peak of the J-band of the TC dye, $\lambda_{TC} = 462$ nm, is situated between the absorption peaks of uncoated 20-nm-radius silver and gold particles: $\lambda_{Ag} = 399$ nm and $\lambda_{Au} = 537$ nm).

A different situation occurs when a metallic (Ag or Au) core is coated with a J-aggregate layer of the PIC dye, which has an oscillator strength of the transition in the J-band an order of magnitude weaker than that for the TC dye (Table 1). Moreover, the wavelength of the unperturbed peak of the J-aggregate, $\lambda_{PIC} = 583$ nm, exceeds those of the two absorption peaks corresponding to the dipole plasmon resonances of silver and gold particles. The absorption peaks of Ag/PIC and Au/PIC particles, which are similar in position to the corresponding unperturbed peaks of the plasmon resonances in Ag and Au, are located in both cases at shorter wavelengths than is the second peak of the hybrid system (Fig. 3). It is seen that, in the former case (Fig. 3a), the difference between the maximum heights of the shorter and longer wavelength peaks is particularly large because of the significant shift, $\Delta\lambda = \lambda_0^J - \lambda_{res}^{Ag}$, of the plasmon resonance peak of uncoated silver particles from the centre of the J-band of the PIC dye. In the latter case (Fig. 3b), the considerably smaller shift, $\Delta\lambda = \lambda_0^J - \lambda_{res}^{Au}$, of the plasmon resonance peak of uncoated gold particles from the absorption peak of the PIC dye J-aggregate leads to equalisation of the maximum heights of the shorter and longer wavelength peaks in the absorption spectrum of Au/PIC particles compared to Ag/PIC particles. Note also that the longer wavelength peak in Fig. 3b is split into two components.

All the solid curves in Figs 2 and 3 were obtained using formulas (1) and (4)–(8) of generalised Mie theory, and the dot-dashed curves were obtained using formulas (9) and (12) of the quasi-static approximation. It follows from comparison of these spectra that the quasi-static approximation allows one to qualitatively account for the behaviour of the photoabsorption spectra, but it fails to provide an adequate quantitative description of the processes under consideration for the particle geometry used ($r_1 = 20$ nm, $l = 3$ nm). This can only be done using the general formulas (1) and (4)–(8) in Section 2.

The discrepancy between the absorption cross sections calculated using exact and approximate formulas increases with increasing outer particle radius r_2. At large r_2, the quasi-static approximation provides no reliable quantitative results and is incapable of accounting for the observed systematic variation of the absorption spectra. Figure 4 presents the calculated absorption cross sections of Ag/TC hybrid particles with various core radii and shell thicknesses. It is seen that, at an outer particle radius $r_2 = 33$ nm (Fig. 4a), there are three photoabsorption peaks in the visible range, in contrast to the two peaks in the spectrum of smaller particles in Fig. 2a. Thus,

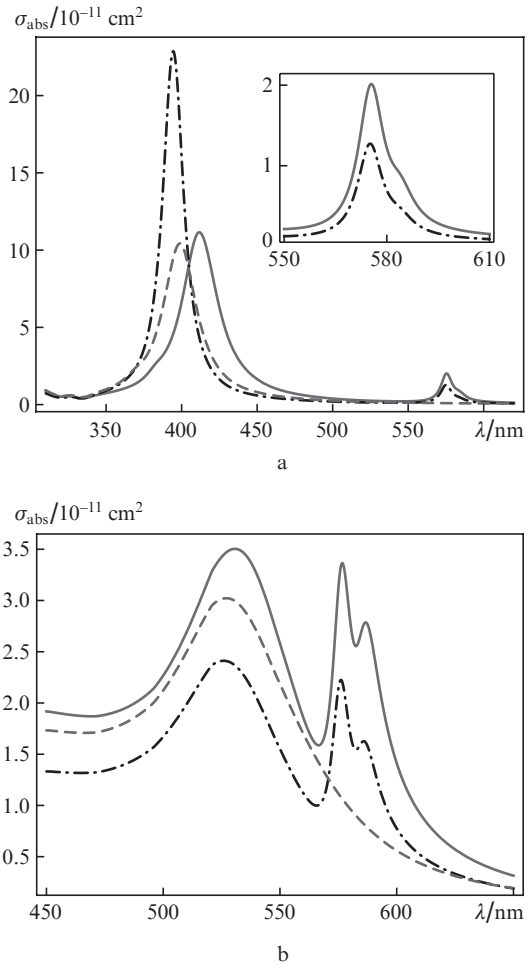

Figure 3. Photoabsorption cross section (σ_{abs}) as a function of wavelength in vacuum (λ) for (a) Ag/PIC and (b) Au/PIC particles in aqueous solution at a core radius $r_1 = 20$ nm and shell thickness $l = 3$ nm (same designations as in Fig. 2).

there is an extra peak near 400 nm. It originates from the excitation of the quadrupole plasmon resonance in the core of hybrid silver particles, which interacts with a Frenkel exciton in the J-aggregate shell. The peaks centred at 429 and 478 nm are due to the coupling between a Frenkel exciton in the shell and the dipole plasmon resonance in the core. Note that, in contrast to the above case (Fig. 2a), the longest wavelength peak in Fig. 4a is markedly stronger than the disturbed dipole and quadrupole plasmon peaks.

Further increasing the particle radius leads to marked changes in the shape of the absorption spectrum. In particular, it causes a significant redistribution of peak heights. This is well illustrated by the calculation results in Fig. 4b (silver core radius $r_1 = 42$ nm, J-aggregate shell thickness $l = 3$ nm). The spectrum has only two peaks in the visible range, but the shorter wavelength peak (near 402 nm) arises from quadrupole plasmon resonance excitation in the particle core (TM mode, $n = 2$). This peak is considerably stronger than that above (Fig. 4a). The middle and shortest wavelength peaks, corresponding to an exciton in the shell and a dipole plasmon in the core interacting with each other, are markedly shifted towards each other to form a single peak centred at $\lambda \approx 470$ nm.

In both cases considered above, the shape of the absorption spectra was governed primarily by the contributions of

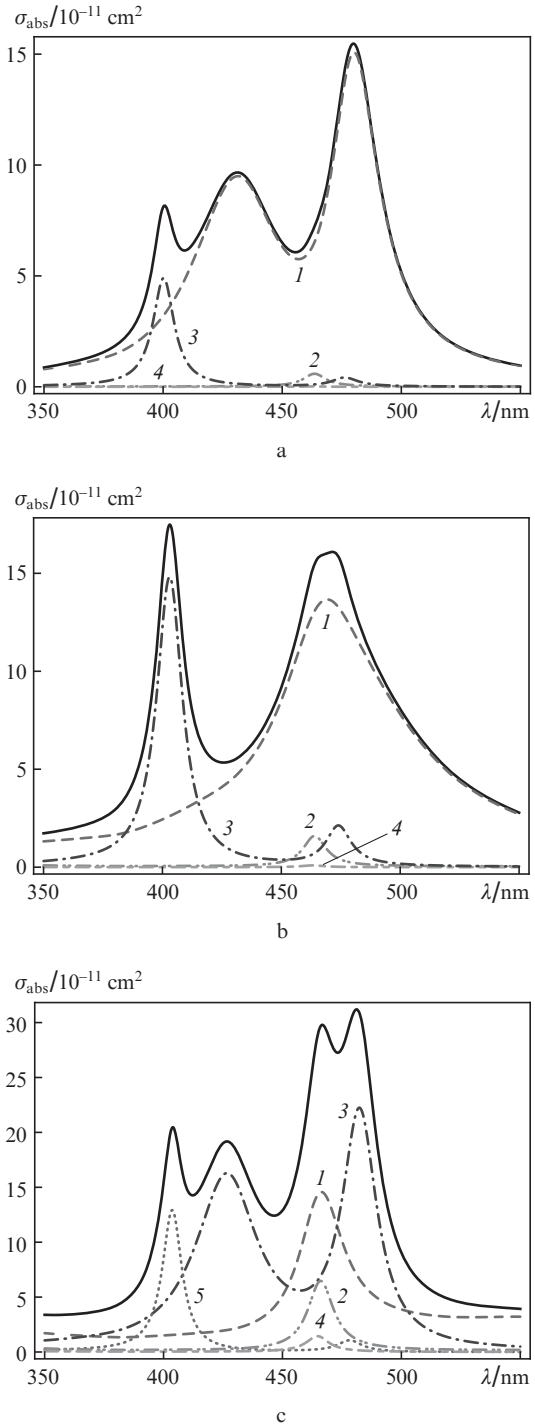

Figure 4. Photoabsorption cross section (σ_{abs}) as a function of wavelength in vacuum (λ) for Ag/TC particles in aqueous solution: (a) r_1 = 30 nm, r_2 = 33 nm; (b) r_1 = 42 nm, r_2 = 45 nm; (c) r_1 = 65 nm, r_2 = 70 nm; the total contribution of all the TM and TE modes (solid lines) and the contributions of the (*1*) electric dipole (TM, n = 1), (*2*) magnetic dipole (TE, n = 1), (*3*) electric quadrupole (TM, n = 2), (*4*) magnetic quadrupole (TE, n = 2) and (*5*) electric octupole (TM, n = 3) modes calculated using the general formulas (1) and (4)–(8).

the TM modes with n = 1 and 2 [Figs 4a, 4b, spectra (*1*), (*3*)], whereas the contribution of the TE modes was extremely small [Figs 4a, 4b, spectra (*2*), (*4*)]. The situation is however more complex when the particle radius exceeds 50 nm. To illustrate the contributions of various electromagnetic field modes to the absorption cross section, Fig. 4c presents relevant calculation results for particles consisting of a silver core of radius r_1 = 65 nm and a J-aggregate shell of thickness l = 5 nm. As seen, the major contributions to the absorption cross section are made by the electric dipole, electric quadrupole and electric octupole modes. Note that, in the cases considered above, the contribution of the octupole TM mode (n = 3) was very small. The contribution of the TE modes does not prevail, as above, but becomes significant. In particular, the largest contribution of the magnetic dipole mode (TE, n = 1) to the absorption cross section is 22% and that of the magnetic quadrupole mode (TE, n = 2) is 5% of the total absorption cross section.

In all the above examples of composite nanoparticles having a silver or gold core, the strongest absorption peaks were situated in the visible range. It is seen in Fig. 5 that, when metal/OC dye J-aggregate particles have a copper or aluminium core, strong photoabsorption peaks emerge in the near-UV spectral region. The reason for this is that the plasmon resonance peaks of isolated copper and aluminium nanoparticles in aqueous solution are located in the near-UV spectral region because the plasma frequencies of Cu and Al (ω_p^{Cu} = 10.8 eV and ω_p^{Al} = 14.5 eV) exceed those of Ag and Au (ω_p^{Ag} = 9.27 eV and ω_p^{Au} = 9.02 eV).

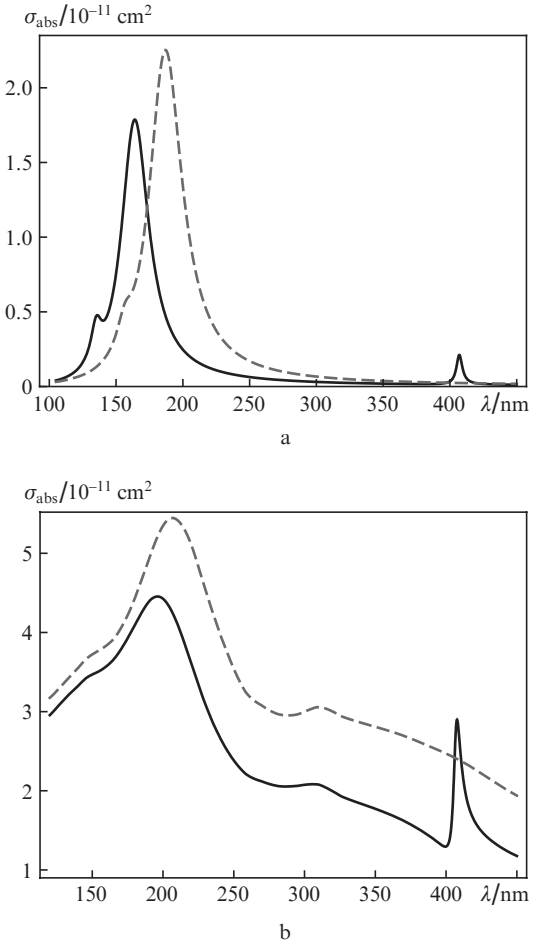

Figure 5. Photoabsorption cross section (σ_{abs}) as a function of wavelength in vacuum (λ) for (a) Al/OC and (b) Cu/OC nanoparticles in aqueous solution at a core radius r_1 = 10 nm and shell thickness l = 3 nm. The solid lines represent calculations by the exact formulas (1) and (4)–(8), and the dashed lines represent calculation results for uncoated aluminium and copper particles (r = 10 nm).

Compare now the present results for uncoated metallic particles and metal/J-aggregate hybrid particles to experimental data and theoretical results in the literature. The solid lines in Fig. 6 represent our results obtained in the framework of generalised Mie theory using frequency- and size-dependent permittivities [formulas (13)–(16)] of Al, Cu, Ag and Au nanoparticles. Figure 6a shows the absorption spectrum of Al calculated by Chowdhury et al. [45], and Fig. 6c presents experimental data for Ag and Au [15]. In both cases, the present calculation results agree well with the data in the literature. In addition, Fig. 6b presents the results of our calculations with the use of the permittivity of bulk copper [spectrum (*2*)], because analogous results are available in the literature [46] [spectrum (*3*)]. It is seen that, in this case as well, the results agree well. Of greatest interest for the purposes of this study is comparison (Fig. 7) of the photoabsorption spectra calculated by us for Ag/TC and Au/TC hybrid nanoparticles (core radius $r_1 = 5$ nm, J-aggregate shell thickness $l = 1$ nm) with relevant experimental data [15] (dot-dashed lines). It follows from this comparison that the calculated spectra successfully reproduce all the key qualitative features in the photoabsorption spectra of the composite nanoparticles under consideration and provide reasonable quantitative results.

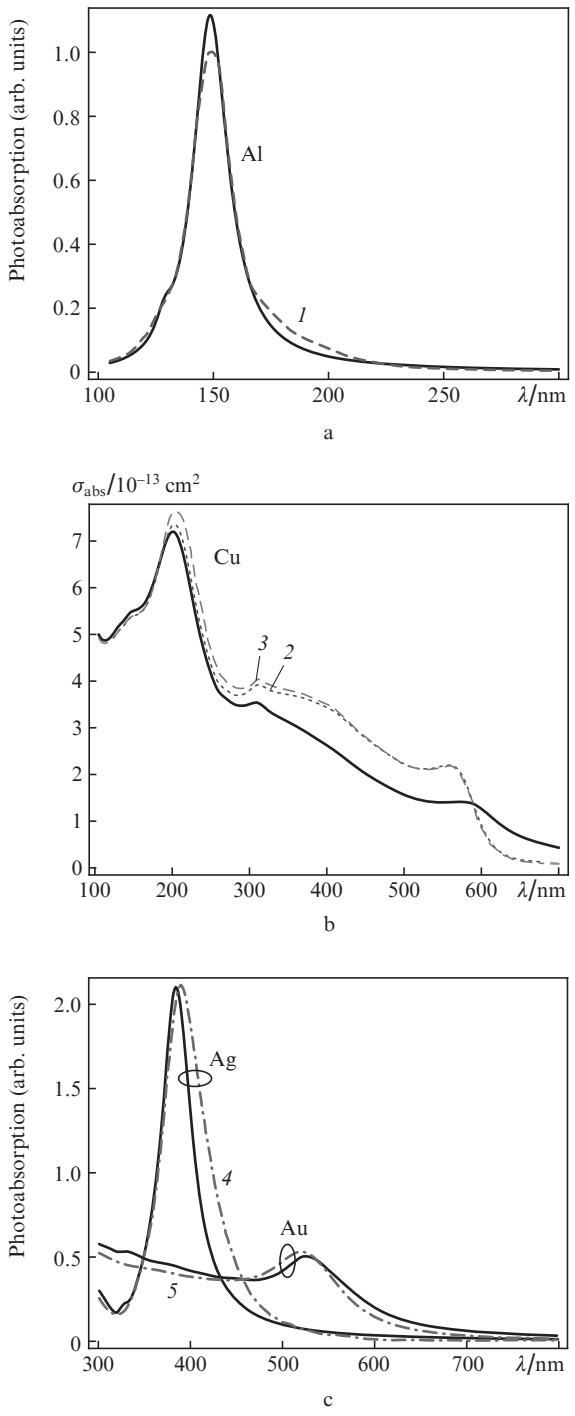

Figure 6. Absorption spectra of Al, Cu, Ag and Au nanoparticles calculated using formulas (1) and (4)–(8) (solid lines) in comparison with available experimental and theoretical results: (a) (*1*) calculated photoabsorption spectrum of 10-nm-radius aluminium particles in air, (b) photoabsorption cross sections calculated (*2*) in this study and (*3*) by Creighton and Eadon [46] for 5-nm-radius copper particles in aqueous solution using the dielectric functions of bulk material and (c) measured photoabsorption spectra of 5-nm-radius (*4*) silver and (*5*) gold particles in aqueous solution [15].

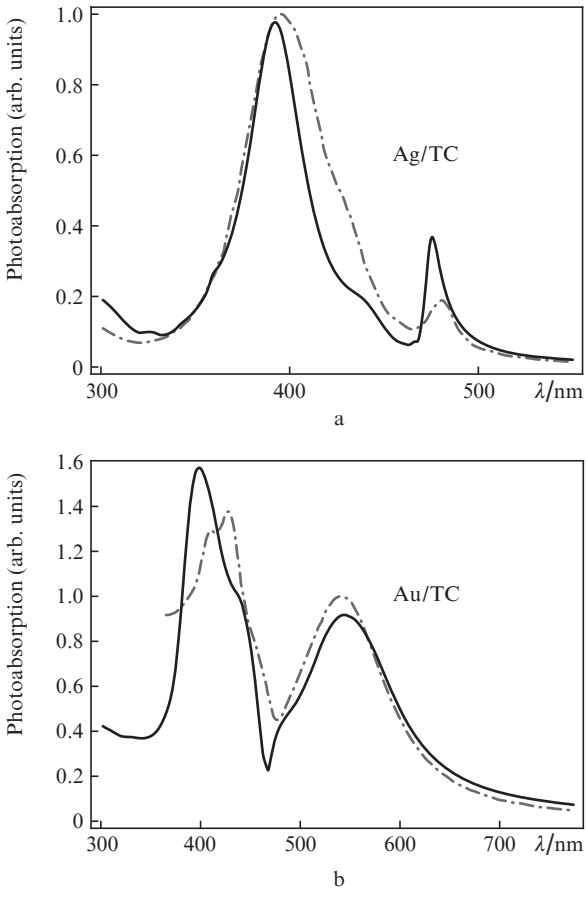

Figure 7. Absorption spectra of (a) Ag/TC and (b) Au/TC hybrid nanoparticles in aqueous solution: calculation in this work by formulas (1) and (4)–(8) (solid lines) and experimental data [15] (dot-dashed lines).

6. Comparison of the light absorption and scattering contributions to the extinction cross section

To assess the relative contributions of light scattering and absorption processes to the total extinction cross section at

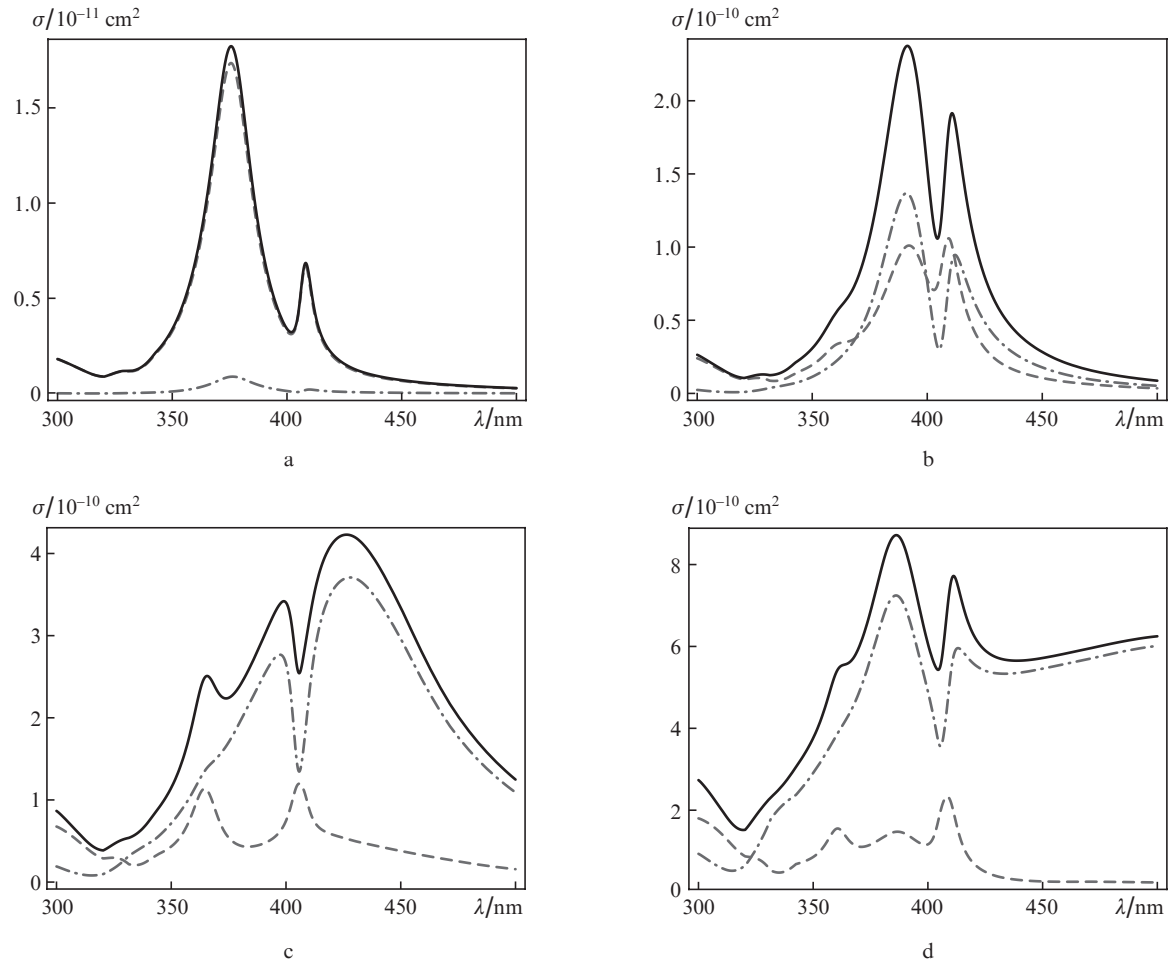

Figure 8. Calculated extinction (solid lines), absorption (dashed lines) and scattering (dot-dashed lines) cross sections of Ag/OC particles in aqueous solution. Geometric parameters of the particles: (a) $r_1 = 10$ nm, $r_2 = 11$ nm; (b) $r_1 = 25$ nm, $r_2 = 27$ nm; (c) $r_1 = 40$ nm, $r_2 = 44$ nm; (d) $r_1 = 65$ nm, $r_2 = 70$ nm.

various sizes of hybrid particles, we performed exact calculations of the cross section for particles consisting of a silver core and OC dye J-aggregate shell. Figure 8 presents the calculation results for four sets of geometric parameters of the system. As in the case of photoabsorption, the scattering spectra of the relatively small particles have two major peaks in the visible range. It is also seen in Fig. 8a that the scattering contribution to the total extinction cross section is negligible compared to the absorption contribution when the particle radius is under 10 nm. The maximum scattering cross section is then 5% of the total extinction cross section.

Increasing the outer particle radius leads to a drastic increase in scattering cross section. This follows directly from comparison of formulas of the quasi-static approximation: $\sigma_{abs} \propto r^3$ and $\sigma_{scat} \propto r^6$ [see (9)]. As a result, when the radius of Ag/TC composite particles increases to 25 nm, the scattering contribution becomes comparable to the photoabsorption contribution (see the dot-dashed and dashed lines in Fig. 8b). At still larger particle sizes, scattering prevails over photoabsorption. Figures 8c and 8d show typical spectral dependences of the extinction cross section under conditions where scattering significantly and greatly prevails over photoabsorption, respectively.

We performed similar calculations for hybrid particles having a gold core. According to the results obtained, the scattering and absorption contributions to the extinction cross section are roughly equal at particle radii from 55 to 60 nm, in contrast to Ag/J-aggregate particles, where this occurs at smaller radii: $r = 25-30$ nm. To more accurately locate the boundary between the regions where light absorption or scattering prevails, one should take into account that it depends on the wavelength of the incident light and the ratio of the shell thickness to the core radius.

7. Analytical model for assessing the frequencies of hybrid modes

The interaction between a surface plasmon in the metallic core and a Frenkel exciton in the shell leads to the formation of plasmon–exciton hybrid states in the composite particle. The frequencies of such hybrid modes and, hence, the spectral position of the corresponding absorption peaks can be approximately determined using an analytical approach: a generalisation of a simple procedure for finding the spectral position of the dipole plasmon resonance in the case of a uniform metallic particle. In this approach, the resonance frequencies of metallic nanoparticles can be found in the quasi-static approximation using the relation $\mathrm{Re}[\varepsilon_m(\omega)] = -2\varepsilon_h$ [see Eqns (9) and (10)]. Substituting relation (13) for the free electron contribution to the permittivity of the metal, ε_m, and neglecting its imaginary part (i.e., taking the attenuation coefficient of plasma oscillations, γ_{intra}, to be zero), we obtain

$\omega_{Fr} = \omega_p/\sqrt{2\varepsilon_h + \varepsilon_m^\infty}$. This is the so-called Frohlich frequency, which determines the position of the resonance dipole plasmon mode of a uniform metallic sphere (see e.g. Ref. [32]).

Similarly, the eigenfrequencies of the hybrid modes of a composite nanoparticle can be found in the quasi-static approximation using the relation $\mathrm{Re}[\varepsilon_2^{\mathrm{eff}}(\omega)] = -2\varepsilon_h$, which contains the effective permittivity $\varepsilon_2^{\mathrm{eff}}$ of a bilayer system [see Eqn (11)]. Further, using Eqns (13) and (17) for the permittivities of the metallic core and J-aggregate shell and taking their imaginary parts to be zero ($\gamma_{\mathrm{intra}} \to 0$ and $\Gamma \to 0$), we obtain the following equation for the eigenfrequencies of the hybrid modes of a metal/J-aggregate bilayer system:

$$C_3x^3 + C_2x^2 + C_1x + C_0 = 0, \quad x = \omega^2. \tag{18}$$

Here, the coefficients C_i depend on the optical constants of the metallic core ($\omega_p, \varepsilon_m^\infty$), J-aggregate shell ($\omega_0, f, \varepsilon_J^\infty$) and environment ($\varepsilon_h$) and the ratio of the radii of the concentric spheres, $\zeta = (r_1/r_2)^3$:

$$C_3 = j(2 + \zeta) + m(1 - \zeta) + k(1 + 2\zeta), \tag{19}$$

$$C_2 = -2(f\varepsilon_h + j)\omega_0^2(2 + \zeta) - 2[(2f\varepsilon_J^\infty + m)\omega_0^2 + \varepsilon_h\omega_p^2](1 - \zeta) - [(f\varepsilon_m^\infty + 2k)\omega_0^2 + \varepsilon_J^\infty\omega_p^2](1 + 2\zeta), \tag{20}$$

$$C_1 = (2f\varepsilon_h + j)(2 + \zeta)\omega_0^4 + [(2f^2 + 4f\varepsilon_J^\infty + m)\omega_0^4 + 4\varepsilon_h\omega_0^2\omega_p^2](1 - \zeta) + [(f\varepsilon_m^\infty + k)\omega_0^4 + (f + 2\varepsilon_J^\infty)\omega_0^2\omega_p^2](1 + 2\zeta), \tag{21}$$

$$C_0 = -\omega_0^4\omega_p^2[2\varepsilon_h(1 - \zeta) + (f + \varepsilon_J^\infty)(1 + 2\zeta)], \tag{22}$$

where

$$j = 2\varepsilon_h\varepsilon_J^\infty; \quad m = 2[(\varepsilon_J^\infty)^2 + \varepsilon_h\varepsilon_m^\infty]; \quad k = \varepsilon_m^\infty\varepsilon_J^\infty. \tag{23}$$

Consider the limiting cases of Eqn (18). If the oscillator strength of the transition in the shell is zero ($f = 0$) and $\zeta \neq 0$, we obtain the following solution:

$$\omega^2 = \frac{\omega_p^2(\delta + \mu\zeta)}{\varkappa + \rho\zeta}, \quad \delta = 2\varepsilon_h + \varepsilon_J^\infty, \quad \mu = 2(\varepsilon_J^\infty - \varepsilon_h), \tag{24}$$

where $\varkappa = 2j + m + k$ and $\rho = j - m + 2k$. Solution (24) corresponds to a metallic particle of radius r_1 and permittivity (13), coated with a passive insulator layer of thickness $l = r_2 - r_1$ and constant permittivity ε_J^∞ and surrounded by a medium of permittivity ε_h. If the shell thickness is $l = 0$, we can take $\zeta = 1$ in (24), which gives $\omega^2 = \omega_p^2/(2\varepsilon_h + \varepsilon_m^\infty)$. This corresponds to the Frohlich frequency ($\omega_{Fr} = \omega_p/\sqrt{3}$ at $\varepsilon_h = \varepsilon_m^\infty = 1$), i.e. to the eigenfrequency of the dipole plasmon resonance mode of a uniform metallic sphere.

Another limiting expression, $\omega^2 = \omega_0^2[1 + f/(2\varepsilon_h + \varepsilon_J^\infty)]$, can be obtained from (18) by taking $\zeta = 0$ ($r_1 = 0$). The frequency defined by this relation coincides with the solution to the equation $\mathrm{Re}[\varepsilon_J(\omega)/\varepsilon_h] = -2$, i.e. it is the resonance frequency of a uniform spherical organic dye particle of permittivity (17). It should, however, be kept in mind that low values of $\zeta = (r_1/r_2)^3$ are of little interest here because we examine plasmon–exciton coupling effects in real physical systems in the form of a metallic core coated with a relatively thin molecular J-aggregate layer.

For further analysis, it is convenient, substituting $y = x + C_2/(3C_3)$, to bring Eqn (18) to the canonical form $y^3 + py + q = 0$, where $p = -a^2/3 + b$, $q = 2(a/3)^3 - ab/3 + c$, and the coefficients $a = C_2/C_3$, $b = C_1/C_3$ and $c = C_0/C_3$ can be found using Eqns (19)–(22). Since all the coefficients C_i, p and q are real numbers, the number of real roots of Eqn (18) depends on the sign of $Q = (p/3)^3 + (q/2)^2$. It follows from the above analysis that Q is negative in all the cases under consideration and, hence, p is also negative. Therefore, Eqn (18) has three different real roots except in the limiting cases $\zeta = 0$ and 1. It is convenient to represent these roots ($x_i \equiv \omega_i^2$) in trigonometric form [47]:

$$\omega_1^2 = -\frac{a}{3} + 2\sqrt{-\frac{p}{3}}\cos\left(\frac{\beta}{3}\right), \qquad \omega_{2,3}^2 = -\frac{a}{3} - 2\sqrt{-\frac{p}{3}}\cos\left(\frac{\beta}{3} \pm \frac{\pi}{3}\right), \tag{25}$$

where $\cos\beta = -q/[2\sqrt{-(p/3)^3}]$. These expressions specify the frequencies of hybrid modes and determine the positions of three peaks in the absorption spectrum of metal/J-aggregate bilayer nanoparticles. Clearly, they are applicable only in the quasi-static approximation and can be used provided that interband transitions in the metallic core make no significant contribution to the permittivity $\varepsilon_m(\omega)$.

The three roots specified by (25) are positive. The root ω_1^2 corresponds to the 'high-energy' hybrid mode of the composite system. The other two roots ($\omega_{2,3}^2$) determine the 'low-energy' and 'medium-energy' modes. According to (19)–(23), the eigenfrequencies of hybrid modes depend on the plasma frequency ω_p, resonance frequency ω_0, reduced oscillator strength f and $\zeta = (r_1/r_2)^3$. As an illustration, we give particular expressions for the coefficients a, b and c in (25) at $\varepsilon_h = \varepsilon_m^\infty = \varepsilon_J^\infty = 1$. We then have $j = 2$, $m = 4$ and $k = 1$, and the relations for a, b and c become significantly simpler:

$$a = -\frac{1}{3}[3(f + 2)\omega_0^2 + \omega_p^2], \quad c = -\frac{\omega_0^4\omega_p^2}{9}[3 + f(1 + 2\zeta)], \tag{26}$$

$$b = \frac{\omega_0^2}{9}\{\omega_0^2[2f^2(1 - \zeta) + 9(f + 1)] + \omega_p^2[f^2(1 + 2\zeta) + 6]\}. \tag{27}$$

In general, the coefficients a, b and c and the frequencies of hybrid modes depend, among other things, on the permittivity of the medium around the particle (ε_h) and the constants ε_m^∞ and ε_J^∞.

8. Effect of the oscillator strength of the transition in the J-band of the dye on hybrid mode frequencies and photoabsorption peak heights

Consider the effect of the reduced oscillator strength, f, of the transition in the J-band of the dye shell on the peak positions and heights in the absorption spectrum of Ag/J-aggregate particles (Figs 9, 10). We performed the corresponding exact numerical calculations for various inner (r_1) and outer (r_2) particle radii at a constant r_1 to r_2 ratio ($r_1/r_2 = 5/6$). Figure 9 shows the hybrid mode frequencies calculated within the

simple analytical model above. All the optical constants of the J-aggregate shell (except for the oscillator strength f) were taken to equal those of the TC dye (see Table 1).

Since the core radius for the curves in Figs 9 and 10 is no greater than 20 nm, none of the high-order (quadrupole, octupole and other) multipole resonances makes a significant contribution to the absorption cross section. Because of this, hybrid modes result here only from the interaction between a Frenkel exciton in the dye J-aggregate shell and a dipole plasmon resonance in the silver core. As would be expected, at $f \neq 0$ the absorption spectrum of the Ag/J-aggregate system shows three distinct peaks, in perfect agreement with the analytical model. As seen in Figs 9 and 10, the oscillator strength has different effects on these peaks. An increase in f leads to a relatively small negative shift of the low-energy peak, whereas the medium- and high-energy peaks undergo positive shifts. For $f \to 0$, the low- and medium-energy peaks shift towards each other to form a single peak. The corresponding maximum absorption cross section tends to zero with decreasing f (Figs 10b, 10c). The frequency of the high-energy peak decreases with decreasing f and at $f = 0$ the peak is located at ~3.3 eV (Fig. 9). The peak height remains nonzero for $f \to 0$ (Fig. 10a). Thus, there is only one absorption peak at $f = 0$. This corresponds to a metallic particle coated with a thin passive layer of constant permittivity ε_J^∞ and surrounded by a medium of permittivity ε_h [see (24) and Fig. 1].

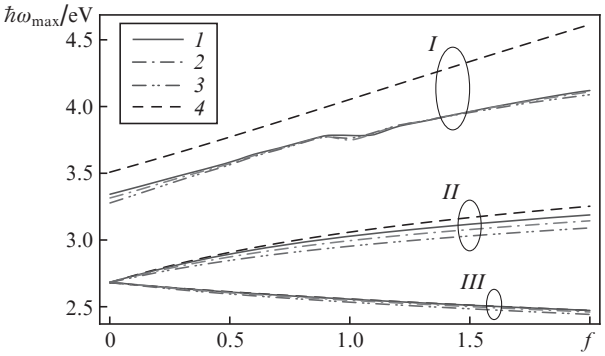

Figure 9. Spectral positions of the (*I*) high-energy, (*II*) medium-energy and (*III*) low-energy absorption peaks vs. reduced oscillator strength f for Ag/J-aggregate particles at the following geometric parameters of the system ($r_1/r_2 = 5/6$): (*1*) $r_1 = 10$ nm, $r_2 = 12$ nm; (*2*) $r_1 = 15$ nm, $r_2 = 18$ nm; (*3*) $r_1 = 20$ nm, $r_2 = 24$ nm. Curves (*4*) represent the analytical results obtained using Eqns (18)–(22).

Comparison of the results presented in Fig. 9 indicates that the proposed analytical model for assessing the frequencies of hybrid modes in nanoparticles provides a rather good description of all the key features in the influence of reduced oscillator strength on the behaviour of absorption peaks. Quantitative discrepancies between the calculations in this model and exact numerical calculations were only found for the high-energy peak, situated near the electronic transitions between the d-valence band and sp-conduction band of silver ($\hbar\omega_g = 3.7$ eV). In this spectral range, the permittivity of silver cannot be adequately described using only the Drude formula. Therefore, to ensure a reliable quantitative description of this hybrid mode at photon energies near the boundary of interband transitions, the analytical approach should be supplemented with adequate evaluation of the bound electron contribution

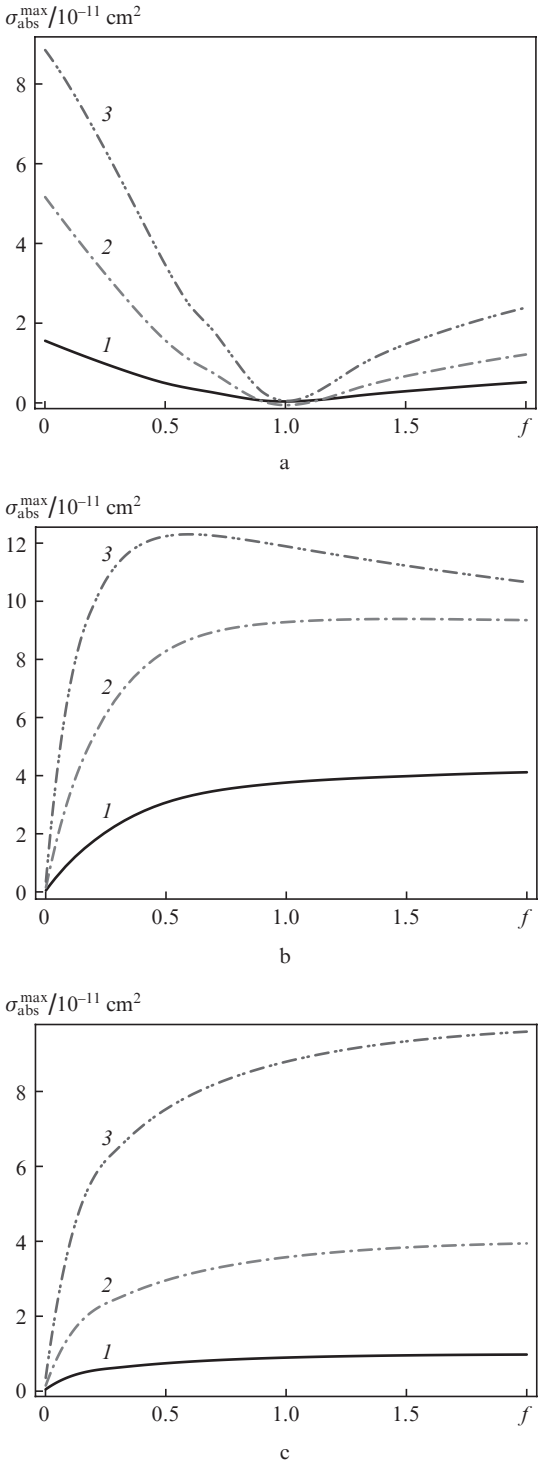

Figure 10. Maximum absorption cross sections of Ag/J-aggregate particles vs. reduced oscillator strength f for the (a) high-energy, (b) medium-energy and (c) low-energy peaks at the following geometric parameters of the system: (*1*) $r_1 = 10$ nm, $r_2 = 12$ nm; (*2*) $r_1 = 15$ nm, $r_2 = 18$ nm; (*3*) $r_1 = 20$ nm, $r_2 = 24$ nm.

to the permittivity. This was done in our exact numerical calculations represented in Figs 9 and 10, which took into account, along with the contribution of interband transitions in Ag, the width of the Γ line of the J-absorption peak of the dye shell and the attenuation coefficients of free (γ_{intra}) and bound (γ_{inter}) electrons in the silver core.

Let us discuss in greater detail the influence of oscillator strength f on the maximum absorption cross section. As mentioned above, the heights of the low- and medium-energy peaks approach zero for $f \to 0$ (Figs 10b, 10c). The height of the low-energy peak increases monotonically with increasing oscillator strength at all the geometric parameters considered. The height of the medium-energy peak increases at $r_1 = 10$ nm, $r_2 = 12$ nm [curve (*1*)] and $r_1 = 15$ nm, $r_2 = 18$ nm [curve (*2*)]. At $r_1 = 20$ nm and $r_2 = 24$ nm [curve (*3*)], the peak height has a maximum at $f = 0.5$ and decreases at higher f values. The height of the high-energy peak at $f = 0$ is the same as that of the plasmon resonance peak of a metallic particle coated with a thin passive layer of constant permittivity ε_J^∞ and surrounded by a medium of permittivity ε_h. The height of this peak decreases with increasing oscillator strength and becomes zero at $f \approx 1.1$ (Fig. 10a). Further increase in f leads to an increase in the height of the high-energy peak. The dip can be accounted for using Eqns (9) and (12) of the quasi-static approximation. At a certain oscillator strength ($f \approx 1.1$), the numerator in the imaginary part of the polarisability of a hybrid particle (and hence its absorption cross section) becomes zero. This occurs at a photon energy $\hbar\omega \approx 3.8$ eV, corresponding to the position of the high-energy peak.

All these general aspects of the light absorption process in Ag/J-aggregate particles are illustrated by Fig. 11, which presents the calculated cross section σ_{abs} as a function of wavelength λ and the oscillator strength f of the transition in the J-band of the dye. It is seen that the low- and medium-energy peaks shift towards each other as f decreases from 3 to 0. The heights of the two peaks decrease and, eventually, they form a single, weak peak centred at $\lambda = 479$ nm, which disappears for $f \to 0$. At the same time, the band located in the UV spectral region shifts to longer wavelengths with decreasing f. At $f = 0$, it peaks at 371 nm. The maximum height of the high-energy peak drops to almost zero at $f = 1.1$ and $\lambda = 325$ nm and then rises again.

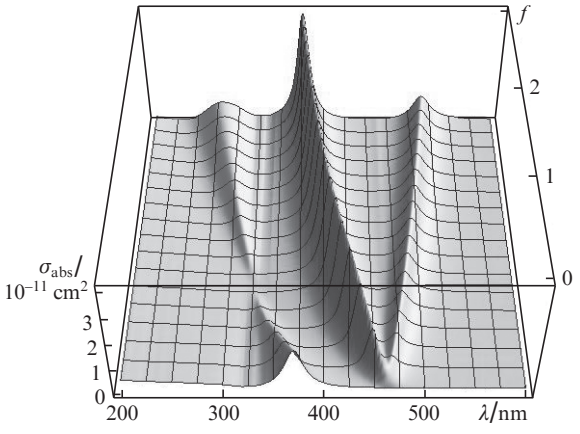

Figure 11. Absorption cross section as a function of wavelength in vacuum (λ) and the reduced oscillator strength (f) of the molecular J-aggregate for Ag/J-aggregate particles in aqueous solution at a core radius $r_1 = 10$ nm and outer particle radius $r_2 = 12$ nm.

The results presented in Fig. 11 were obtained for a relatively small particle ($r_1 = 10$ nm, $r_2 = 12$ nm), with spectral behaviour determined by the interaction between a Frenkel exciton and a dipole plasmon. At considerably larger particle radii, Frenkel excitons interact with both dipole and quadrupole plasmons. This causes several additional peaks to emerge in the photoabsorption spectrum of the hybrid nanoparticles. This effect is illustrated in Fig. 12, which shows the absorption cross section as a function of wavelength λ and oscillator strength f for Ag/J-aggregate particles with geometric parameters $r_1 = 30$ nm and $r_2 = 33$ nm.

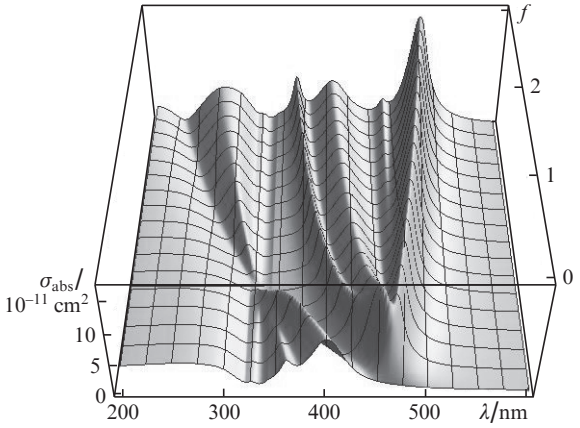

Figure 12. Absorption cross section as a function of wavelength in vacuum (λ) and the reduced oscillator strength (f) of the molecular J-aggregate for Ag/J-aggregate particles in aqueous solution at a core radius $r_1 = 30$ nm and outer particle radius $r_2 = 33$ nm.

9. Conclusions

We have calculated the light absorption and scattering cross sections of metallic (Ag, Au, Cu and Al) nanoparticles coated with different cyanine dyes. The results indicate that the number of peaks in the extinction spectra of the nanoparticles depends on their geometric parameters and the optical constants of the core and shell materials and the peaks may differ little or strongly in height (Figs 2–4). This is because plasmon–exciton coupling in such systems has different effects in the weak and strong coupling regimes.

Particular attention has been paid to size effects. Their influence on the optical properties of metal/J-aggregate systems strongly depends on the outer radius of the particle, r_2. In the limit of small r_2, the absorption cross section is determined by the contribution of the electric dipole term and can be adequately described within the quasi-static approximation. The scattering contribution to the extinction cross section is then negligible (Fig. 8a). In addition to the obvious increase in cross section with increasing particle volume ($\sigma_{abs} \propto r_2^3$), the size effect on the absorption spectrum then reduces to two factors.

First, because of the electromagnetic core–shell coupling, the polarisability of the hybrid system depends not only on the permittivities of the core and shell but also on the ratio of the inner and outer radii of the concentric spheres, $(r_1/r_2)^3$ [see Eqns (9) and (12)]. Therefore, varying this ratio allows peak positions and heights in the extinction spectrum of composite particles to be tuned over rather wide ranges.

Second, the permittivity of a core depends on it size because, in contrast to that of bulk metal, the permittivity ε_{intra} is modified in this case. This is due to free electron scattering by the surface of the metallic core. The effect is particu-

larly strong when the particle radius is much less than the electron mean free path l_∞ in bulk metal. In the case of hybrid particles with a silver core, this effect has a strong influence on the width and height of spectral peaks when the particle radius ($r \sim 5$ nm) is an order of magnitude smaller than $l_\infty^{Ag} = 52$ nm. The size effect in particles with a gold core is significant but weaker than that in particles with a silver core. This is mainly due to the smaller electron mean free path in bulk gold: $l_\infty^{Au} = 13$ nm.

The simple formulas (9) and (12) of the quasi-static approximation are incapable of providing an adequate quantitative description of the absorption process when the particle size exceeds 10–15 nm (Figs 2, 3). Still larger particles have more complex photoabsorption spectra because of the influence of additional multipole plasmon resonances. This fact can be illustrated by the example of the absorption spectra of Ag/TC particles with $r_2 = 33$ nm (Fig. 4a). In addition to the peaks that result from the interaction of a Frenkel exciton with a dipole plasmon in the hybrid system, the spectra contain a peak due to the excitation of a quadrupole plasmon in the metallic core. In the examples considered above, this peak was strongest at $r_2 = 45$ nm (Fig. 4b).

A number of extra features in the extinction spectra of the particles result from the competition between the absorption and scattering contributions as the particle size increases (Fig. 8). The extinction cross section of silver particles coated with a dye J-aggregate is determined mainly by absorption at an outer radius under 25–35 nm, and the scattering contribution prevails at larger particle radii. In the case of hybrid particles with a gold core, the scattering contribution prevails at outer particle radii $r_2 \gtrsim 55$–60 nm.

Our calculations demonstrate that the hybrid mode frequencies of a composite nanoparticle, which determine peak positions in its absorption and scattering spectra, strongly depend on the reduced oscillator strength f of the transition in the J-band of the organic dye (Fig. 9). Changes in f lead to a significant redistribution of peak heights (Fig. 10). We have identified spectral and oscillator strength ranges where the photoabsorption has minima and maxima (Figs 11, 12). In addition, we have demonstrated significant changes in the absorption and extinction spectra of metal/J-aggregate nanoparticles in response to changes in core radius and shell thickness. All this indicates the possibility of controlling the efficiency and nature of plasmon–exciton coupling and tailoring the optical properties of hybrid nanoparticles.

Acknowledgements. This work was supported by the Russian Foundation for Basic Research (Grant No. 12-02-00713-a) and the Physical Sciences Division of the Russian Academy of Sciences (programmes 'Fundamental Optical Spectroscopy and Its Applications' and 'Fundamental Aspects of the Physics and Technology of Semiconductor Lasers As Cornerstones of Photonics and Quantum Electronics').

References

1. Wood V., Panzer M.J., Caruge J.-M., Halpert J.E., Bawendi M.G., Bulović V. *Nano Lett.*, **10**, 24 (2010).
2. Brown P.R., Lunt R.R., Zhao N., Osedach T.P., Wanger D.D., Chang L.-Yi., Bawendi M.G., Bulović V. *Nano Lett.*, **11**, 2955 (2011).
3. Yatsui T., Sangu S., Kawazoe T., Ohtsu M., An S.J., Yoo J., Yi G.-C. *Appl. Phys. Lett.*, **90**, 223110 (2007).
4. Ohtsu M. (Ed.) *Nanophotonics and Nanofabrication* (Weinheim: Wiley-VCH Verlag GmbH & Co. KgaA, 2009).
5. Cai W., Shalaev V. *Optical Metamaterials: Fundamentals and Applications* (New York: Springer, 2010).
6. Hill M.T. et al. *Nat. Photonics*, **1**, 589 (2007).
7. Zimmler M.A., Bao J., Capasso F., Müller S., Ronning C. *Appl. Phys. Lett.*, **93**, 051101 (2008).
8. Ambati M., Nam S.H., Ulin-Avila E., Genov D.A., Bartal G., Zhang X. *Nano Lett.*, **8**, 3998 (2008).
9. Noginov M.A., Zhu G., Belgrave A.M., Bakker R., Shalaev V.M., Narimanov E.E., Stout S., Herz E., Suteewong T., Wiesner U. *Nature*, **460**, 1110 (2009).
10. Biju V., Itoh T., Anas A., Sujith A., Ishikawa M. *Anal. Bioanal. Chem.*, **391**, 2469 (2008).
11. Oldenburg S.J., Averitt R.D., Westcott S.L., Halas N.J. *Chem. Phys. Lett.*, **288**, 243 (1998).
12. Prodan E., Nordlander P. *J. Chem. Phys.*, **120**, 5444 (2004).
13. Brandl D.W., Mirin N.A., Nordlander P. *J. Phys. Chem. B*, **110**, 12302 (2006).
14. Shapiro B.I. *Usp. Khim.*, **75**, 484 (2006) [*Russ. Chem. Rev.*, **75**, 433 (2006)].
15. Kometani N., Tsubonishi M., Fujita T., Asami K., Yonezawa Y. *Langmuir*, **17**, 578 (2001).
16. Sato T., Tsugawa F., Tomita T., Kawasaki M. *Chem. Lett.*, **30**, 402 (2001).
17. Hranisavljevic J., Dimitrijevic N.M., Wurtz G.A., Wiederrecht G.P. *J. Am. Chem. Soc.*, **124**, 4536 (2002).
18. Wurtz G.A., Hranisavljevic J., Wiederrecht G.P. *J. Microsc.*, **210**, 340 (2003).
19. Wiederrecht G.P., Wurtz G.A., Hranisavljevic J. *Nano Lett.*, **4**, 2121 (2004).
20. Wiederrecht G.P., Wurtz G.A., Bouhelier A. *Chem. Phys. Lett.*, **461**, 171 (2008).
21. Lebedev V.S., Vitukhnovsky A.G., Yoshida A., Kometani N., Yonezawa Y. *Colloids Surf. A: Physicochem. Eng. Aspects*, **326**, 204 (2008).
22. Lebedev V.S., Medvedev A.S., Vasil'ev D.N., Chubich D.N., Vitukhnovsky A.G. *Kvantovaya Elektron.*, **40**, 246 (2010) [*Quantum Electron.*, **40**, 246 (2010)].
23. Uwada T., Toyota R., Masuhara H., Asahi T. *J. Phys. Chem. C*, **111**, 1549 (2007).
24. Wurtz G.A., Evans P.R., Hendren W., Atkinson R., Dickson W., Pollard R.J., Zayats A.V. *Nano Lett.*, **7**, 1297 (2007).
25. Yoshida A., Yonezawa Y., Kometani N. *Langmuir*, **25**, 6683 (2009).
26. Shapiro B.I., Kol'tsova E.S., Vitukhnovsky A.G. *Ross. Nanotekhnol.*, **6**, 83 (2011).
27. Mastroianni A.J., Claridge S.A., Alivisatos A.P. *J. Am. Chem. Soc.*, **131**, 8455 (2009).
28. Fan J.A., He Y., Bao K., Wu C., Bao J., Schade N.B., Manoharan V.N., Shvets G., Nordlander P., Liu D.R., Capasso F. *Nano Lett.*, **11**, 4859 (2011).
29. Pillai S., Catchpole K.R., Trupke T., Zhang G., Zhao J., Green M.A. *Appl. Phys. Lett.*, **88**, 161102 (2006).
30. Catchpole K.R., Polman A. *Opt. Express*, **16**, 21793 (2008).
31. Atwater H.A., Polman A. *Nat. Mater.*, **9**, 205 (2010).
32. Bohren C.F., Huffman D.R. *Absorption and Scattering of Light by Small Particles* (New York: Wiley, 1983; Moscow: Mir, 1986).
33. Aden A.L., Kerker M. *J. Appl. Phys.*, **22**, 1242 (1951).
34. Güttler A. *Ann. Phys. (Leipzig)*, **11**, 65 (1952).
35. Ruppin R., Englman R. *J. Phys. C*, **1**, 630 (1968).
36. Fuller K.A. *Opt. Lett.*, **18**, 257 (1993).
37. Irimajiri A., Hanai T., Inouye A. *J. Theor. Biol.*, **78**, 251 (1979).
38. Kreibig U., Vollmer M. *Optical Properties of Metal Clusters* (Berlin: Springer, 1995).
39. Pines D., Nozieres P. *Theory of Quantum Liquids* (New York: Benjamin, 1966; Moscow: Mir, 1967).

40. Johnson P.B., Christy R.W. *Phys. Rev. B*, **6**, 4370 (1972).
41. Palik E.D. (Ed.) *Handbook of Optical Constants of Solids II* (San Diego: Academic Press, 1991).
42. Kay G.W.C., Laby T.H. *Tables of Physical and Chemical Constants* (Essex–New York: Longman Scientific & Technical, 1995).
43. Yoshida A., Kometani N. *J. Phys. Chem. C*, **114**, 2867 (2010).
44. Owens R.W., Smith D.A. *Langmuir*, **16**, 562 (2000).
45. Chowdhury M.H., Ray K., Gray S.K., Pond J., Lakowicz J.R. *Anal. Chem*., **81**, 1397 (2009).
46. Creighton J.A., Eadon D.G. *J. Chem. Soc., Faraday Trans*., **87**, 3881 (1991).
47. Korn G.A., Korn T.M. *Mathematical Handbook for Scientists and Engineers* (New York: McGraw-Hill, 1961; Moscow: Nauka, 1973).